nature photonics

SUPPLEMENTARY INFORMATION

https://doi.org/10.1038/s41566-017-0012-4

In the format provided by the authors and unedited.

$Cs_2AgBiBr_6$ single-crystal X-ray detectors with a low detection limit

Weicheng Pan[1,2], Haodi Wu[1,2], Jiajun Luo[1,2], Zhenzhou Deng[3,4], Cong Ge[1,2], Chao Chen[1,2], Xiaowei Jiang[5,6], Wan-Jian Yin[5,6], Guangda Niu[1,2]*, Lujun Zhu[7], Lixiao Yin[1,2], Ying Zhou[1,2], Qingguo Xie[4]*, Xiaoxing Ke[7], Manling Sui[7] and Jiang Tang[1,2]*

[1]Wuhan National Laboratory for Optoelectronics (WNLO), Huazhong University of Science and Technology (HUST), 430074 Wuhan, China. [2]School of Optical and Electronic Information, Huazhong University of Science and Technology (HUST), 430074 Wuhan, China. [3]School of Information Engineering, Nanchang University, 330031 Nanchang, China. [4]School of Life Science and Technology, Huazhong University of Science and Technology, 430074 Wuhan, China. [5]Soochow Institute for Energy and Materials InnovationS (SIEMIS), College of Physics, Optoelectronics and Energy & Collaborative Innovation Center of Suzhou Nano Science and Technology, Soochow University, 215006 Suzhou, China. [6]Key Laboratory of Advanced Carbon Materials and Wearable Energy Technologies of Jiangsu Province, Soochow University, 215006 Suzhou, China. [7]Institute of Microstructure and Property of Advanced Materials, Beijing University of Technology, 100124 Beijing, China. Weicheng Pan, Haodi Wu, Jiajun Luo and Zhenzhou Deng contributed equally to this work. *e-mail: guangda_niu@mail.hust.edu.cn; qgxie@mail.hust.edu.cn; jtang@mail.hust.edu.cn

Supplementary materials online

$Cs_2AgBiBr_6$ single crystal X-ray detector with a low detection limit

Weicheng Pan[1,2†], Haodi Wu[1,2†], Jiajun Luo[1,2†], Zhenzhou Deng[3,4†], Cong Ge[1,2], Chao Chen[1,2], Xiaowei Jiang[5,6], Wan-Jian Yin[5,6], Guangda Niu[1,2*], Lujun Zhu[7], Lixiao Yin[1,2], Ying Zhou[1,2], Qingguo Xie[4*], Xiaoxing Ke[7], Manling Sui[7], Jiang Tang[1,2*]

[1]Wuhan National Laboratory for Optoelectronics (WNLO), and [2] School of Optical and Electronic Information, Huazhong University of Science and Technology (HUST), Wuhan, 430074, China

[3]School of Information Engineering, Nanchang University, Nanchang, 330031, China.

[4]School of Life Science and Technology, Huazhong University of Science and Technology, Wuhan 430074, China.

[5]Soochow Institute for Energy and Materials InnovationS (SIEMIS), College of Physics, Optoelectronics and Energy & Collaborative Innovation Center of Suzhou Nano Science and Technology, and [6]Key Laboratory of Advanced Carbon Materials and Wearable Energy Technologies of Jiangsu Province, Soochow University, Suzhou 215006, China.

[7]Institute of Microstructure and Property of Advanced Materials, Beijing University of Technology, Beijing 100124, China.

[†]These authors contributed equally to this work.

Correspondence and requests for materials should be addressed to G. N., Q. X., and J. T.

(E-mail: guangda_niu@mail.hust.edu.cn; qgxie@mail.hust.edu.cn; jtang@mail.hust.edu.cn)

Contents

S1. XRD patterns of $Cs_2AgBiBr_6$ powders

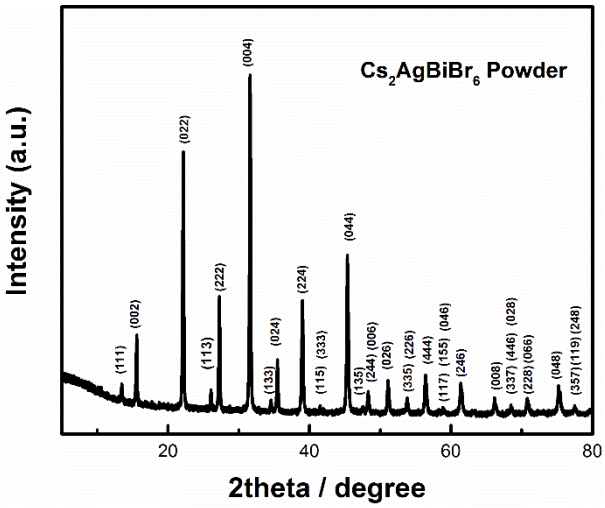

Figure S1 | Powder XRD patterns of $Cs_2AgBiBr_6$. Sample was prepared by grinding the $Cs_2AgBiBr_6$ SC into fine powders and then subjected to standard XRD measurement. All diffraction peaks agreed very well with the previous reported diffraction pattern of cubic $Cs_2AgBiBr_6$.[1]

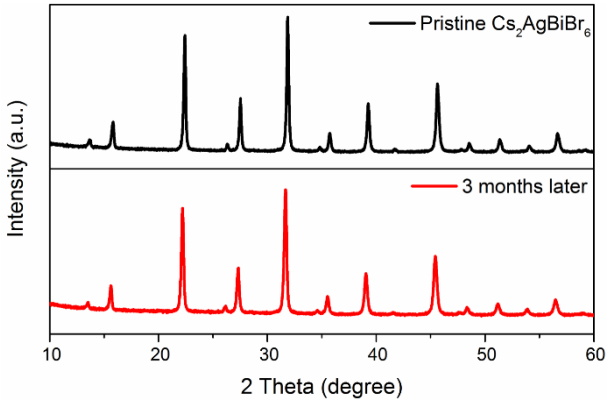

Figure S2 | Powder XRD patterns of $Cs_2AgBiBr_6$ stored for 3 months in air (relative humidity ~60%).

S2. SAED patterns of $Cs_2AgBiBr_6$

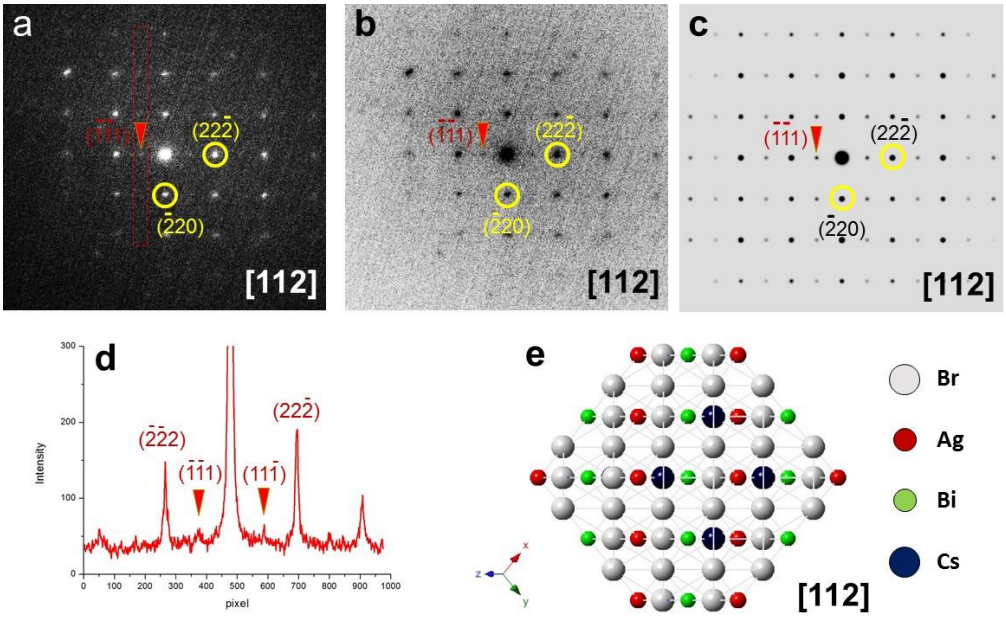

Figure S3| a, Selected area electron diffraction (SAED) pattern of $Cs_2AgBiBr_6$ from [112] zone axis. SAED patterns were obtained on a Titan G2 microscope operating at 300 kV. **b,** The SAED pattern of (a) reversed in contrast to demonstrate better the presence of (111) diffraction spot. **c,** Simulated electron diffraction pattern from the ideal structure of $Cs_2AgBiBr_6$. **d,** Line profile of the diffraction spot intensity along the red dashed box as shown in (a), which indicates the presence of (111) reflection. **e,** Illustration of the ordered structure viewed from [112] direction, where the alternative arrangement of Ag and Bi is clearly demonstrated.

S3. Effect of surface treatment

Different solvents, including acetone, isopropanol, ethanol, ethyl acetate and n-octylamine, were used to rinse the $Cs_2AgBiBr_6$ single crystal and then dried in vacuum. Au electrodes were thermally evaporated on the crystal surface to construct a Au/$Cs_2AgBiBr_6$/Au device for dark conductivity and photoresponse measurement. Illumination was generated by a diode with light emitted at 530 nm at an intensity of 2.48 mW cm^{-2}. Table 1 summarized the dark current and photocurrent at 1 V. After surface treatment, the contacts changed from poor ohmic to perfect ohmic, and dark currents were significantly decreased except for octylamine treated sample. In addition, isopropanol, ethanol and ethyl acetate were found to retain or even enhance the photocurrents. Considering both the change of dark current and photocurrent, we chose

isopropanol as the best solvent for treatment. We believe surface rinse could remove adsorbed chemicals (HBr and $BiBr_3$, as show in the ICP-MS test)-induced surface states on the crystal and reduce the surface conduction effect. Besides, surface treatment also suppressed the Schottky barrier between pristine $Cs_2AgBiBr_6$ SCs and gold electrodes.

Table 1. Dark and photocurrent of the $Cs_2AgBiBr_6$ SC devices with different solvent treatments.

treatment	Dark current (pA)	Photocurrent (nA)
Acetone	31	14.9
Isopropanol	76	90.0
Ethanol	62	70.0
Ethyl acetate	23	55.1
n-Octylamine	850	88.9
Control	1100	52.3

In order to prove the role of surface treatment on removing surface defects, a control experiment was conducted by firstly evaporating gold electrodes onto opposite sides of one $Cs_2AgBiBr_6$ single crystal, and then rinsing the crystal with isopropanol. Hypothetically the trap states would be retained between $Cs_2AgBiBr_6$ SCs and gold electrodes, while surface defects in the uncovered region would be removed. As supposed, the resistivity was indeed increased from 5.42×10^{10} Ω cm to 9.29×10^{10} Ω cm and the Schottky barrier still existed after this treatment.

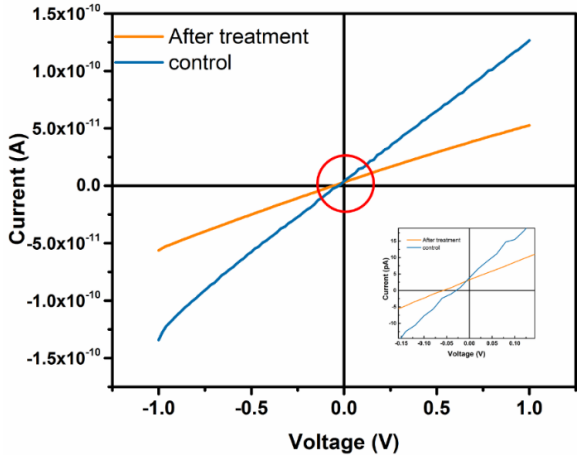

Figure S4 | I-V curves of the Au/$Cs_2AgBiBr_6$/Au device. Control was the device using unwashed $Cs_2AgBiBr_6$ SCs. Treatment meant rinse of the whole Au/$Cs_2AgBiBr_6$/Au device with isopropanol. As enlarged in the inset, both I-V curves didn't pass through the origin, indicating the presence of a weak Schottky barrier between Au electrodes and pristine

$Cs_2AgBiBr_6$ SC.

To understand the contaminants on the surface of the crystal, we collected the isopropanol after rinsing and subjected this solvent for inductively coupled plasma mass spectrometry (ICP-MS) analysis, a technique that is very sensitive to metallic elements. As shown in the following table, it was found Bi ions presented in isopropanol after washing. Thereby, we believe the contaminant of the surface could be $BiBr_3$, one of the precursors. In addition, HBr may also adsorb on the surface and could be removed after isopropanol treatment.

Table 2. ICP-MS analysis results of elements in isopropanol

	Ag (mg/L)	**Bi (mg/L)**
Isopropanol after washing	<0.05	2.864
Isopropanol before washing	<0.05	<0.05

S4. Comparison of SC resistivity between $Cs_2AgBiBr_6$ and $MAPbBr_3$ SCs

Following the method stated above, we have measured the dark I-V curves of a bunch of $Cs_2AgBiBr_6$ and $MAPbBr_3$ SCs and then calculated the resistivity. As listed in Table 3, $Cs_2AgBiBr_6$ SCs consistently showed much larger resistance than $MAPbBr_3$ SCs, with the averaged value being three orders of magnitude larger.

Table 3. The measured resistivity of $Cs_2AgBiBr_6$ and $MAPbBr_3$ SCs

No.	$Cs_2AgBiBr_6$ Ω cm	$MAPbBr_3$ Ω cm
1	1.051×10^{10}	2.411×10^{7}
2	5.567×10^{9}	2.840×10^{7}
3	7.400×10^{9}	2.189×10^{7}
4	1.60×10^{11}	1.835×10^{7}
5	9.062×10^{9}	1.455×10^{7}
6	6.738×10^{9}	7.291×10^{6}
Average	3.321×10^{10}	1.907×10^{7}

S5. Characterization of the trap density and mobility of $Cs_2AgBiBr_6$ SCs

Space charge-limited current (SCLC) analysis was applied to obtain the trap density and carrier mobility of our $Cs_2AgBiBr_6$ SCs. Device configuration was Au/$Cs_2AgBiBr_6$ SC/Au. Dark

current-voltage measurements were conducted using Agilent B1500A, and the non-linear I-V curves were analyzed according to the SCLC model. Three different regimes exist in the curve, i.e. Ohmic ($I \propto V^{n=1}$), trap-filled ($I \propto V^{n>3}$), and Child's ($I \propto V^{n=2}$) regime. The critical point from Ohmic to trap-filled regime is known as trap-filled limit voltage. The relationship between the trap density and the onset voltage of the trap-filled-limit (TFL) regime is expressed as:

$$V_{TFL} = \frac{en_t L^2}{2\varepsilon\varepsilon_0}$$

where ε_0 is the vacuum permittivity, ε is the relative dielectric constant, n_t is the trap density, L is the thickness of SCs. ε is obtained by measuring the capacitance between two electrodes, as detailed in next section. When operating in Child's regime, I-V curve follows the Mott-Gurney law:

$$J_D = \frac{9}{8}\varepsilon\varepsilon_0\mu\frac{V^2}{L^3}$$

Where μ is the carrier mobility and V is the bias voltage. Thereby, we could estimate the carrier mobility in this region.

S6. Characterization of the dielectric constant of $Cs_2AgBiBr_6$ SC

We built a simple plate capacitor to measure the dielectric constant of our $Cs_2AgBiBr_6$. Device configuration was again Au/$Cs_2AgBiBr_6$ /Au where the $Cs_2AgBiBr_6$ SC was served as the dielectric layer. By measuring the capacitance-frequency at dark, as shown in Figure S6, we could obtain the relative dielectric constant of $Cs_2AgBiBr_6$ using the parallel plate capacitor model:

$$C = \varepsilon\varepsilon_0 S/D$$

where S is the electrode area (3.14 mm^2), D is the thickness of SCs (2.5 mm).

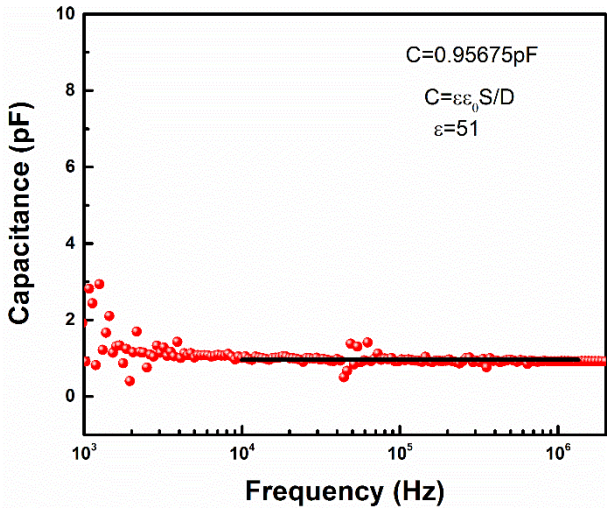

Figure S5 | Capacitance of Au/$Cs_2AgBiBr_6$/Au parallel plate capacitor.

S7. Characterization of the photoconductivity of $Cs_2AgBiBr_6$ SC

Photoconductivity measurement was carried out on the $Cs_2AgBiBr_6$ SC device with the structure of Au/$Cs_2AgBiBr_6$ SC/Au. A modified Hecht equation was used to fit the obtained result, deriving the information of μτ product and surface recombination velocity *s*.

$$\mathrm{I} = \frac{I_0 \mu \tau V}{L^2} \frac{1 - exp\left(-\frac{L^2}{\mu \tau V}\right)}{1 + \frac{L}{V}\frac{s}{\mu}}$$

where I_0 is the saturated photocurrent, L is the thickness, V is the applied bias, τ is the carrier lifetime. The fitting curve was shown in Figure 2f.

S8. Characterization of the responsivity, EQE, -3dB of $Cs_2AgBiBr_6$ SC photodetectors

The -3 dB cutoff frequency was measured to obtain the response time of the planar structured photodetectors (**Figure S6a)**. The device was illuminated by a LED with a wavelength of 530 nm with varied switching frequency. The -3dB cutoff frequency at 6 V bias was 1300 Hz (0.77 ms). The high responsivity and response time could match those of $MAPbX_3$ SCs. Then the responsivity (R) and external quantum efficiency (EQE) were measured. The R is defined as the ratio of total photocurrent to incident light intensity, and can be calculated as:

$$R = \left(I_p - I_d\right)/(A \cdot P)$$

where I_p is photocurrent, I_d is dark current, A is the photo active area of the device and P

is the incident light intensity. EQE is calculated as:

$$EQE = \frac{R \cdot hc}{e\lambda}$$

where R is the responsivity, h is Planck's constant, c is the velocity of light, e is the electronic charge and λ is the wavelength of the incident light. $Cs_2AgBiBr_6$ SCs-based detector before thermal annealing showed a R of 3.38 ~0.04 A/W and EQE of 793%~9.6% within the incident light intensity ranging from 0.04532 to 47280 μW cm^{-2} at 1V bias. After thermal annealing, the performance of the detector significantly increased, with R reaching 15.04~0.067 A/W and EQE of 3525%~15.6%. We could further measure the detectivity (D*) of our device by the following equation: $D^* = (Af)^{1/2}R/i_n$ where A is the effective area of the detector and i_n is the noise current. Using the procedure stated in the main text, we measured the noise of this planar photoconductive photodetector as i_n=6.69 × 10^{-15} A/$Hz^{1/2}$ at 34Hz and finally calculate the D* of our device as 1.60×10^{13} Jones.

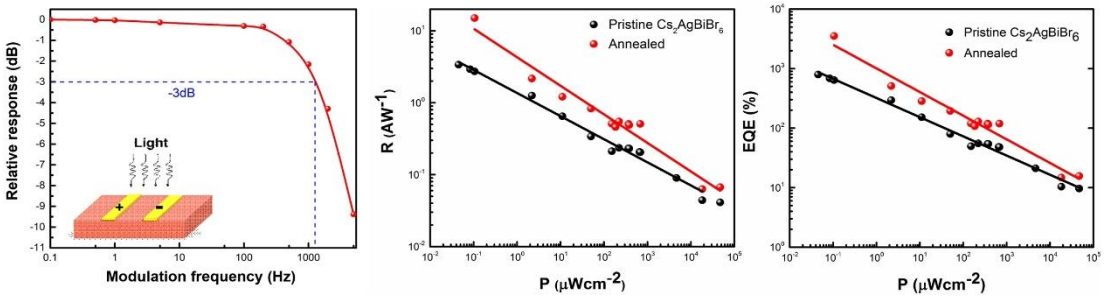

Figure S6 | The performance of our $Cs_2AgBiBr_6$ SC-based photodetectors. a, Normalized response of the detector versus the input signal frequency (light intensity of 1.27 mW cm^{-2}) at a bias voltage of 6 V. The -3dB point is marked with the dash line. **b,** Light intensity-dependent responsivity for the detectors before and after thermal annealing. **c,** Calculated external quantum efficiency.

S9. X-ray tube equipment and dose rate calibration

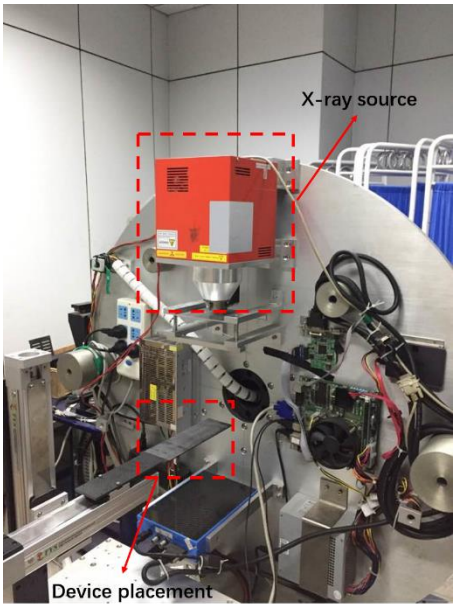

Figure S7 | Tungsten anode X-ray tube used in this work. The tube was operated at 50 kV and 2 mm Al foil served as an attenuator.

Accurate calibration of X-ray dose rate is compulsory to obtain credible results. It should be noted that we should be careful about the working mechanisms of the commercial dosimeters. Basically, counting mode and integrating mode are two mechanisms for dosimeters. Counting mode is designed to record each individual quantum of radiation that interacts in the detector. However, for high dose rates, counting mode operation becomes impractical or even impossible. The time between adjacent events may become too short to carry out an adequate analysis, or the current pulses from successive events may overlap in time. Thereby, for high dose rate of x-rays, counting mode may lead to deviations from the real value. In contrast, for integrating mode, the detectors will integrate the generated charge in a selected time window. The read was proportional to the X-ray tube current, and the concept of 'dead time' is not applicable to such dose meter. We applied two commercial X-ray dosimeters, which are in integrating mode, to measure the dose rate where the detection limit of our $Cs_2AgBiBr_6$ SC detector was measured: Si detector (model: RaySafe X2 R/F) from Fluke and Ion chamber (model: 10X6-180) from Radcal. The results are listed in Table 4. Please note that for ion chamber, the dose rate was directly obtained from the reading. However, for Si detector, the dose rate was extrapolated following the $1/r^2$ (r: distance from the X-ray tube) law by measuring the dose rate at a distance

with stronger X-ray intensity. We adopted the data measured by ion chamber from Radcal and used this number for the calculation of detection limit of our $Cs_2AgBiBr_6$ SC detectors. We also applied the data measured by the ion chamber to calibrate the X-ray dose rate when the X-ray tube operated at different currents, and at different positions. All device performance presented in the manuscript is calculated based on the values measured by Radcal ion chamber.

Table 4. Measured dose rate by different dosimeters

Detector	Dose (nGyair/s)	Measurement
Fluke (Si)	56.3	Extrapolated value
Radcal (Ion chamber)	59.7	Direct measurement

S10. Calculation of signal-to-noise ratio.

As shown in Fig 3f, the signal current (I_{signal}) was derived by subtracting the average photocurrent ($\bar{I}_{photo}$) by the average dark current ($\bar{I}_{dark}$). The noise current (I_{noise}) was obtained by calculating the standard deviation of the photocurrent.

$$I_{signal} = \bar{I}_{photo} - \bar{I}_{dark}$$

$$I_{noise} = \sqrt{\frac{1}{N}\sum_{i}^{N}(I_i - \bar{I}_{photo})^2}$$

Then the signal-to-noise ratio (SNR) was calculated as:

$$\mathrm{SNR} = I_{signal}/I_{noise}$$

For example, for $Cs_2AgBiBr_6$ SC device with 5 V bias and under 59.7 nGy_{air} s^{-1}, the calculated average photocurrent, dark current, and noise current was 0.422 pA, 9.762 pA, and 0.114 pA, respectively, resulting in a SNR value of 3.70.

S11. Calculation of the detection limit of our $Cs_2AgBiBr_6$ SC detector in terms of X-ray photons per second per mm^2 (cps/mm^2)

In order to compare the detection limit with a signal of a single X-ray photon, we performed the following calculations to understand the detection limit of our **$Cs_2AgBiBr_6$ SC detector** in

terms of cps/mm^2:

Method 1: We have estimated the X-ray fluence by using the software (SPEKTR3.0) which is kindly shared by the I-STAR lab at John-Hopkins University and can be freely downloaded from http://istar.jhu.edu/downloads/. As our X-ray tube voltage is operated at 50 kV and filtered by a 2 mm Al foil and assume the kV ripple as 0 % (the input parameter for the software), the fluence is integrated as 16609644 photons/mGy/mm^2 following the "TASMICS" (tungsten anode spectral model using interpolating cubic splines) method. Since the lowest detectable is 59.73 nGy$_{air}$/s, we can calculate the corresponding minimum number of photons discernable by our $Cs_2AgBiBr_6$ single crystal detector as:

$$N = 59.73\ \mathrm{nGy_{air}/s} \times 16609644\ \ \mathrm{photons/mGy/mm^2} = 992\ \mathrm{cps/mm^2}$$

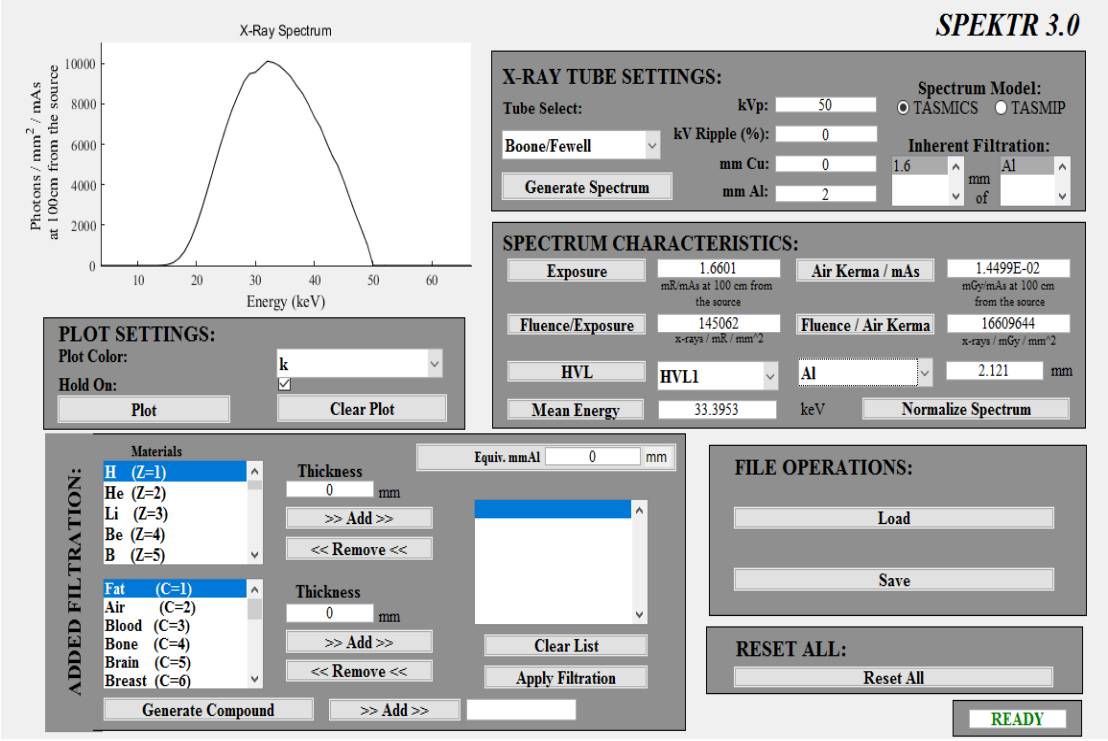

Figure S9| The software window and input parameters for calculation.

Method 2: For a mono-energetic X-ray beam, the number of photons per unit of exposure can be calculated as derived by Johns[2]:

$$\frac{\Phi}{X} = \frac{5.43 \times 10^5}{(\mu[E]/\rho)_{\mathrm{en}} E}\ \frac{\mathrm{photons}}{\mathrm{mm^2 mR}}$$

where $(\mu[E]/\rho)_{\mathrm{en}}$ is the energy-dependent mass energy absorption coefficient for air, Φ is

the photon fluence (photons/mm^2), X is the exposure (mR) and E is X-ray energy. Thanks to the works of John M. Boone and J. Anthony Seibert[2], we can refer to some selected values of Φ/X in the table and calculate the number of photons. As the mean energy of our X-ray beam is 30 keV, the Φ/X is 123632 photons/mm^2/mR. Since 1 mR=8.9×10^{-6} Gy and the detection limit of our detector is 59.7 nGy$_{air}$/s (which is equal to 6.71 x 10^{-3} mR), we can calculate the number of minimum detectable photons as:

$$N = 6.71 \times 10^{-3}\ \text{mR} \times 123632\ \text{photons/mm}^2/\text{mR} = 829\ \text{cps/mm}^2$$

Please note we assume the X-ray beam to be mono-energetic (30 keV) for this calculation.

Table 5. The Φ/X values adopted from Table III in the reference[3]

Energy (keV)	Φ/X	Energy (keV)	Φ/X
1	153	60	303 591
5	2 894	65	307 196
10	12 141	70	305 707
15	28 667	75	295 162
16	33 169	80	283 525
17	37 252	85	271 075
18	42 843	90	258 864
19	47 298	95	246 611
20	53 832	100	235 671
21	58 892	105	222 517
22	66 034	110	210 627
23	71 395	115	200 019
24	78 444	120	190 296
25	86 495	125	181 353
30	123 632	130	173 019
35	168 450	135	165 227
40	210 747	140	157 904
45	248 464	145	151 174
50	277 068	150	144 913
55	295 723		

Method 3: In the work by John M. Boone and J. Anthony Seibert[3], they also presented a fitting function to calculate the photon fluence which have considered the tube operational voltage (kV), the added aluminum filtration (mm Al) and the ripple (%).

$$y = \mathrm{a} + \mathrm{b}x + \mathrm{c}x^2 + \mathrm{d}x^3$$

$$\mathrm{a} = -8270.266\,843\,782\,573$$

$$\mathrm{b} = 90\,292.88\,218\,322\,948$$

$$\mathrm{c} = -11\,567.16\,891\,240\,857$$

$$\mathrm{d} = 541.6\,101\,860\,864\,931$$

where y is the photon fluence in units of photons/mR/mm^2, x is the HVL (half value layer) in the units of mm Al, and $\mathrm{a}, \mathrm{b}, \mathrm{c}, \mathrm{d}$ are constants. As the HVL is 2.2 mm Al for our X-ray tube, we have calculated the photon fluence as 140153 photons/mR/mm^2. We can estimate the discernable X-ray quanta of our $Cs_2AgBiBr_6$ X-ray detector as:

$$N = 6.71 \times 10^{-3}\ \mathrm{mR} \times 140153\ \mathrm{photons/mm^2/mR} = 940\ \mathrm{cps}/mm^2$$

S12. Characterization of the copper tube by our $Cs_2AgBiBr_6$ SC detector

The experiment was used to demonstrate that $Cs_2AgBiBr_6$ SC detector can inspect thick industrial products or detect cracks in steels thanks to its ultralow detection limit. The application of a copper tube is to simulate the voids or flaws in a thick metal component. The copper tube had an inner diameter of 10.4 mm and outer diameter of 13.0 mm. We conducted the experiment by inserting or removing the copper tube between the detector and X-ray tube, and then recording the resulted current response of $Cs_2AgBiBr_6$ SC and $MAPbBr_3$ SC detector. The reference $MAPbBr_3$ SC detector (Au/$MAPbBr_3$ SC/Au) used $MAPbBr_3$ SC with a $\mu\tau$ product of 1.4×10^{-2} cm^2 V^{-1} and surface recombination velocity of 1245 cm s^{-1}. Both detectors were operated at identical external bias. As shown in Figure 3h, there was no response from $MAPbBr_3$ control device, while $Cs_2AgBiBr_6$ device still responded under the same testing conditions.

S13. Characterization of the activation energy for ionic transport in $Cs_2AgBiBr_6$ and $MAPbBr_3$ SCs

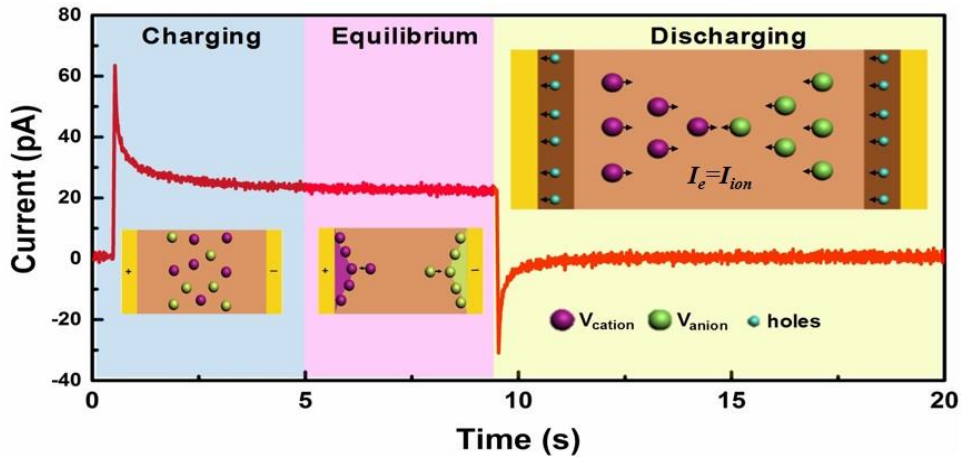

Figure S10 | Schematic illustrations and the representative curve for a typical charging-discharging process for $Cs_2AgBiBr_6$ SC device measured at 253 K.

We adopted the strategy first demonstrated by Duan et. al. to measure the ionic migration in our $Cs_2AgBiBr_6$ SC.[4] As shown in Figure S11, two symmetric Au electrodes were evaporated onto the SCs to eliminate the influence of built-in electric field from asymmetric contacts. Upon exerting a dc bias, electronic current was immediately observed, as evidenced by the current spike. Meanwhile, cation and anion vacancies (V_{Br}, V_{Ag} and so on) moved following the direction of external electric field, gradually accumulated at the $Cs_2AgBiBr_6$/Au electrode interface, creating an internal field that partially cancels the external bias and reduces the electronic current until reaching a steady state. This was the equilibrium with the $Cs_2AgBiBr_6$ bulk fully depleted at this equilibrium. When the external bias was turned off, ion vacancies would promptly migrate backwards because of the large concentration gradient, forming an ionic current in an opposite direction. Majority carriers, holes in our case, would also inject into the $Cs_2AgBiBr_6$ to turn the previously depleted region into the neutral region, resulting in the electronic current with the same direction as the ionic current. Ionic current and electronic current superimposed into the largest negative current instantly after the bias was off, showing as the negative current spike. The countercurrent I was expressed as:

$$I = I_{ion} + I_e$$

where I_{ion} is the ionic current and I_e is the electronic current. Since hole injection strictly depended on the amplitude and speed of ion vacancies retraction, electronic current and ionic current were identical in terms of direction and amplitude, which could be expressed as $I_e =$

I_{ion}. As ion concentration gradient gradually decreased, ion migration also weakened and the kinetics of ions movement were fully reflected by the decay of negative countercurrent. Thereby the measured current *I* is proportional to I_{ion} ($I \propto I_{ion}$). By fitting the current decay curve with an exponential function, we can attribute the decay lifetime (τ) to the ion restoration process. Thus the decay rate represents the ionic transport dynamics and is proportional to the ionic conductivity (σ_{ion}).

Here the temperature dependent ionic conductivity was addressed as:

$$\sigma_{ion} = ne\mu = \frac{Z_i e^2 C_v D_v}{k_B T} \quad (1)$$

where Z_i is the number of the ionic charge, N_A is Avogadro constant, k_B is Boltzmann constant, C_v is the concentration of vacancy, D_v is the diffusion coefficient of vacancy. D_v can be expressed by following formula:

$$D_v = D_v^0 \exp\left(-\frac{E_a}{k_B T}\right) \quad (2)$$

where E_a is the diffusion barrier for ion migration and D_v^0 is a constant. Considering the Schottky equilibrium of intrinsic vacancies creation, C_v could be deduced according to the following equations[5]:

$$2V_{Cs} + V_{Ag} + V_{Bi} + 6V_{Br} = null \quad (3)$$

From the equation above, we can deduce that:

$$[V_{Cs}]^2 \cdot [V_{Ag}] \cdot [V_{Bi}] \cdot [V_{Br}]^6 = K_s = K_s^0 \exp\left(-\frac{\Delta H_s}{k_B T}\right) \quad (4)$$

where K_s is the Schottky constant, ΔH_s is the formation energy of ionic vacancy of eq. (3) and K_s^0 is a constant. Since the lattice points is maintained constant, we have:

$$[V_{Cs}] = 2[V_{Ag}] = 2[V_{Bi}] = \frac{1}{3}[V_{Br}] \quad (5)$$

From eq. (3)-(5), we have:

$$C_v = [V_{Br}] = (324K_s^0)^{(1/10)} \exp\left(-\frac{\Delta H_s}{10k_B T}\right) = C_v^0 \exp\left(-\frac{\Delta H_s}{10k_B T}\right) \quad (6)$$

So, eq. 1 can be expressed as:

$$\sigma_{ion} = \frac{Z_i e^2 C_v^0 D_v^0}{k_B T} \exp\left(-\frac{\Delta H_s}{10k_B T}\right) \exp\left(-\frac{E_a}{k_B T}\right) \quad (7)$$

Through transformation, we obtain:

$$\sigma_{ion}T = \frac{Z_i e^2 C_v^0 D_v^0}{k_B} \exp\left(-\frac{\Delta H_s}{10k_BT} - \frac{E_a}{k_BT}\right) = \sigma_0 \exp\left(-\frac{E_a^{eff}}{k_BT}\right) \quad (8)$$

where the E_a^{eff} the effective activation energy for ion transport considering the contribution from both vacancy formation and vacancy migration.

At last, since the decay rate k (τ^{-1}) is proportional to the ionic conductivity σ_{ion}, eq. (8) could be transformed as:

$$kT \propto \sigma_0 \exp\left(-\frac{E_a^{eff}}{k_BT}\right) \quad (9)$$

$$\ln(kT) = C - \frac{E_a^{eff}}{k_BT} \quad (10)$$

where C is a fitting constant. From eq. (10), we could derive the activation energy (E_a^{eff}) by fitting the Arrhenius plots of $\ln(kT)$ versus $1/T$. In this work, the counter currents versus time with temperature ranging from 253 to 286 K were used for ionic migration study. Some representative curves for discharging process of $Cs_2AgBiBr_6$ were shown in Figure S11, respectively.

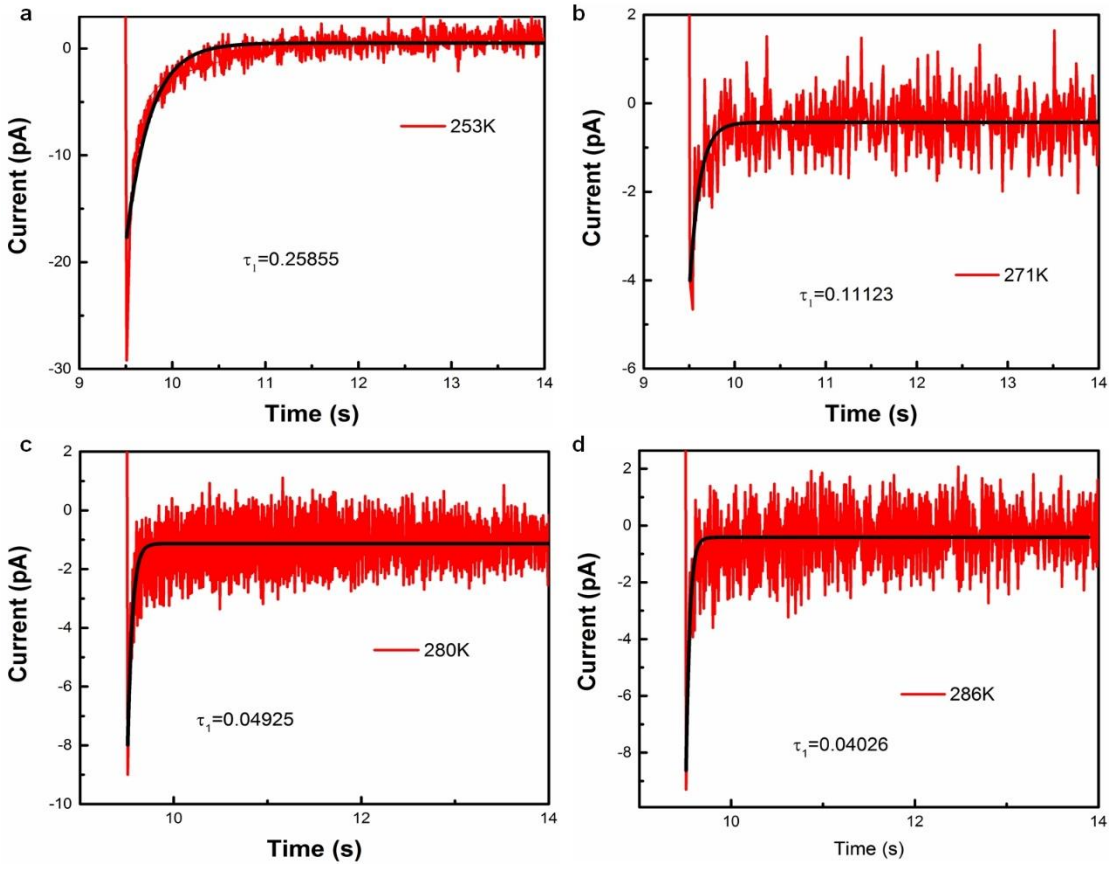

Figure S11 | The representative temporal response curves of $Cs_2AgBiBr_6$ SCs for discharging stage at various temperatures: **a,** 253 K; **b,** 271 K; **c,** 280 K; **d,** 286 K. The measurements were conducted in dark conditions.

References

(1) A. H. Slavney, T. Hu, A. M. Lindenberg, H. I. Karunadasa, *J. Am. Chem. Soc.* **2016**, *138*, 2138.
(2) H. E. Johns, J. R. Cunningham. The Physics of Radiology. (Thomas, Springfield, IL, 1974.
(3) J. M. Boone, J. A. Seibert. *Med. Phys*, **1997**, *24*, 1661.
(4) D. Li, H. Wu, H-C. Cheng, G. Wang, Y. Huang, X. Duan, *ACS nano* **2016**, *10*, 6933.
(5) J. Mizusaki, K. Arai, K. Fueki, *Solid State Ionics* **1983**, *11*, 203.